Superlattices in van der Waals materials: a low-energy electron microscopy study

Jong, T.A. de

6

IMAGING MOIRÉ DEFORMATION AND DYNAMICS IN TWISTED BILAYER GRAPHENE

In 'magic angle' twisted bilayer graphene (TBG) a flat band forms, yielding correlated insulator behavior and superconductivity. In general, the moiré structure in TBG varies spatially, influencing the overall conductance properties of devices. Hence, to understand the wide variety of phase diagrams observed, a detailed understanding of local variations is needed.

Here, we study spatial and temporal variations of the moiré pattern in TBG using aberration-corrected Low Energy Electron Microscopy (AC-LEEM). We find a smaller spatial variation than reported previously. Furthermore, we observe thermal fluctuations corresponding to collective atomic displacements over 70 pm on a timescale of seconds. Remarkably, no untwisting is found up to 600 °C.

We conclude that thermal annealing can be used to decrease local disorder. Finally, we observe edge dislocations in the underlying atomic lattice, the moiré structure acting as a magnifying glass. These topological defects are anticipated to exhibit unique local electronic properties.

Parts of this chapter have been published as T. A. de Jong, T. Benschop, X. Chen, E. E. Krasovskii, M. J. A. de Dood, R. M. Tromp, M. P. Allan and S. J. van der Molen, Nat. Commun. **13**, 70 (2022) [135].

6.1 INTRODUCTION

In twisted bilayer graphene (TBG) a moiré pattern forms that introduces a new length scale to the material. At the 'magic' twist angle $\theta_m \approx 1.1°$, this causes a flat band to form, yielding emergent properties such as correlated insulator behavior and superconductivity [4, 5, 155, 156]. In general, the moiré structure in TBG varies spatially, influencing the local electronic properties [157–161]. This has clear consequences for charge transport experiments, where a percolative average of the microscopic properties is measured. Local variation in twist angle and strain in TBG will directly influence the result of such experiments. In particular, to understand the wide variety observed in the phase diagrams and critical temperatures, a more detailed understanding of the local moiré variation is needed [162].

However, imaging such microscopic variations is non-trivial. A myriad of experimental techniques has been applied to the problem [106, 120, 151, 163–166], each only resolving part of the puzzle due to practical limitations (capping layer or device substrate, surface quality or measurement speed).

Here, we use aberration-corrected Low Energy Electron Microscopy (AC-LEEM) [25, 27], which measures an image of the reflection of a micron-sized beam of electrons at a landing energy E_0 (0–100 eV, referenced to the vacuum energy) in real space, in reciprocal space (diffraction), or combinations thereof. This allows us to perform large-scale, fast and non-destructive imaging of TBG, including device-scale moiré images and dynamics on timescales of seconds. Additionally, spectroscopic measurements, yielding information on the material's unoccupied bands can be done by varying E_0 [29, 34].

Using AC-LEEM to image moiré patterns enables high temperature imaging and has the benefit no suspended samples are required, like they are for TEM-based techniques. This means that sample geometries closely resembling device geometries can be imaged, including devices with leads. Even though not shown here, imaging the moiré pattern through a capping layer of hBN would be possible, although this would be limited to an very thin capping layer of at most a few atomic layers (where SEM-based techniques have demonstrated imaging through much thicker layers [166]).

At 500 °C, we observe thermal fluctuations of the moiré lattice, corresponding to collective atomic displacements of less than 70 pm on a time scale of seconds [167]. Despite previous concerns, no untwisting of the layers is found, even at temperatures as high as 600 °C [112, 168]. Finally, we report the existence of individual edge dislocations in the atomic and moiré lattice.

6.2 RESULTS

A schematic of a TBG sample as used in this work is shown in Figure 6.1**a**. In Figure 6.1**b**, LEEM spectra are shown, taken on several locations of such a TBG sample. These LEEM spectra are directly related to layer count, as described in Refs. [31, 34, 46, 169]; on the one hand via interlayer resonances in the 0–5 eV range, on the other hand via the gradual disappearance of a minimum at 8 eV. Here, more graphene layers (having a band gap at 8 eV) are progressively masking an hBN band underneath. This allows us to determine the local graphene layer count for each point on our sample. To visualize that, we choose three characteristic energies, i.e. $E_0 = 4$ eV (red), $E_0 = 8$ eV (green) and $E_0 = 17$ eV (blue)

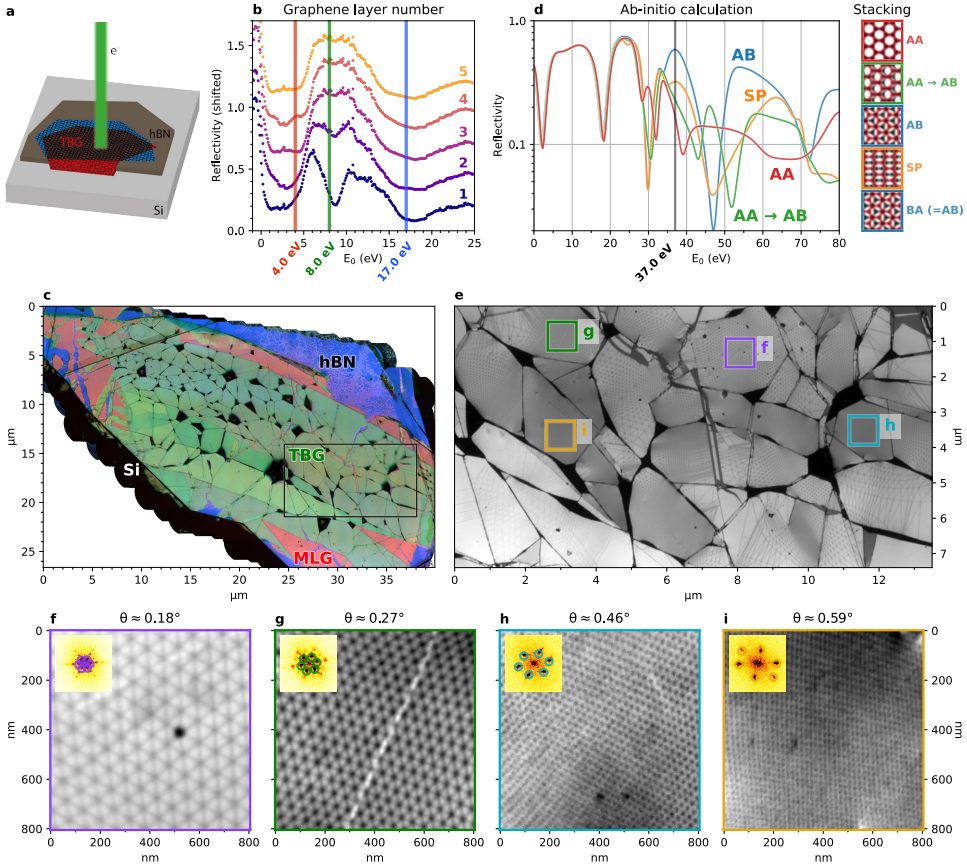

Figure 6.1: Device-scale imaging of TBG. ***a,*** *Schematic of the sample, with two twisted graphene flakes (TBG) on top of an hexagonal boron nitride (hBN) flake on a silicon (Si) substrate.* ***b,*** *Local spectra used to determine the graphene layer count. Vertical lines indicate the imaging energies used for panel c, number of graphene layers is indicated on the right.* ***c,*** *Stitched composite bright field overview of a sample using 4 eV, 8 eV and 17 eV as imaging energies in red, green and blue respectively (see main text for color interpretation). Visible defects include folds in black, tears, where the monolayer (red/pink, indicated as MLG) or even bare hBN (blue, purple) shines through, bubbles (bright) and some polymer residue in the lower and upper right (dark speckles). The black rectangle indicates the area shown in panel d.* ***d,*** *Ab-initio calculations of LEEM spectra of different relative stackings of bilayer graphene, 37 eV indicated.* ***e,*** *Stitched bright field overview of the same sample imaged at $E_0 = 37$ eV, for optimal stacking contrast, revealing the moiré patterns.* ***f-i,*** *Crops of different twist angles areas from* ***e,****. Insets show Fourier transforms and the detected moiré peaks, with the average twist angle θ extracted from those indicated. All data shown in the main text have been collected from the sample represented in panel* ***c****.*

(as indicated in Figure 6.1**b**), and combine stitched overviews at these energies into a single false-color image (Figure 6.1**c**). This overview confirms that the sample consists of large TBG areas (darker green in Figure 6.1**c**) surrounded by monolayer graphene (pink),

on an hBN flake (blue/purple) on silicon (black). Stripes of brighter green indicate areas of 2-on-2 graphene layers (lower stripe), 2-on-1 (upper stripe), and 1-on-2 (wedge on the lower right). The relatively homogeneous areas are themselves separated by folds, appearing as black lines. The folds locally combine in larger dark nodes (confirmed by AFM, See Figure C.8 in Appendix C). A few folds, however, have folded over and appear as lines of higher layer count. Hence, Figure 6.1**c** provides a remarkable overview of a larger-scale sample, with detailed local information.
Increasing E_0 beyond 25 eV, stacking boundaries and AA-sites become visible [37, 169]. This is consistent with ab-initio calculations of LEEM spectra for different relative stackings, as presented in Figure 6.1**d**. Therefore, imaging at $E_0 = 37$ eV (indicated in Figure 6.1**d**) yields a precise map of the moiré lattice over the full TBG area (see Figure 6.1**e**). We find that separate areas, between folds, exhibit different moiré periodicities and distortion [170]. This allows us to study different moiré structures on a single sample. Figure 6.1**f-i** shows full resolution crops of areas indicated in Figure 6.1**e**. The observed twist angles on this sample range from $< 0.1°$ to $0.7°$. For smaller angles, we observe local reconstruction towards Bernal stacking within the moiré lattice, consistent with literature [120, 165]. The best resolution was reached on another sample with a twist angle of $1.3°$ (See Figure 6.2).

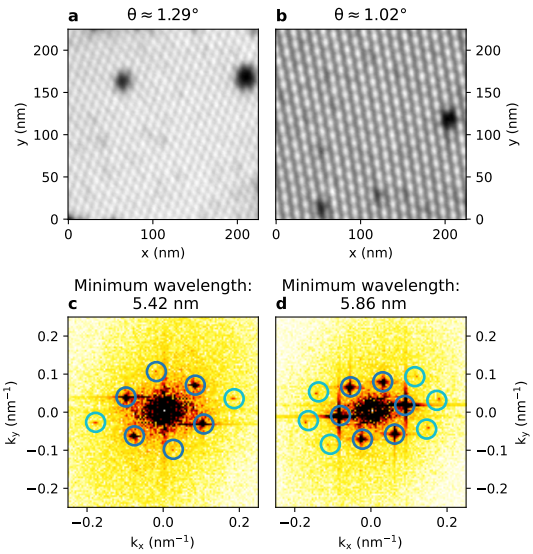

Figure 6.2: ***a,b,*** *Images of 2-on-2 layer twisted graphene at E_0 = 17.0 eV, with twist angles of respectively $\theta \approx 1.29°$ and $\theta \approx 1.02°$* ***c,d,*** *FFTs of the images in a and b respectively, with Bragg peaks corresponding to the moiré pattern indicated in blue. Higher order moiré peaks are also visible (indicated in cyan), corresponding to minimum detectable wavelengths of less than 6 nm.*

6.2.1 DISTORTIONS & STRAIN

The moiré patterns shows distortions, corresponding to local variations in twist angle and (interlayer) strain. Near folds, for instance, the strain increases resulting in strongly elongated triangles, for example in the lower right corner of Figure 6.1**d** [171]. Despite their relative homogeneity, the moiré areas in Figure 6.1**f-i** also show subtle distortions. As structural variations correlate directly with local electronic properties, we quantify

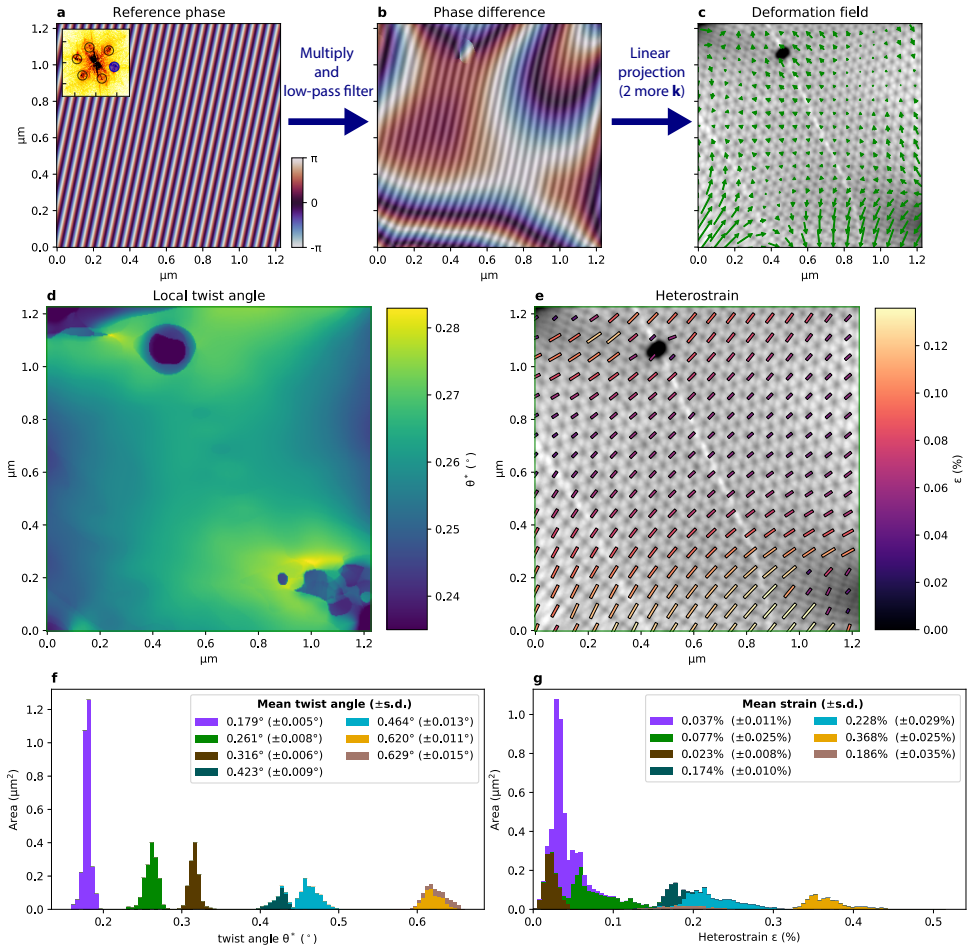

Figure 6.3: Distortion variation from Geometric Phase Analysis. a, *Reference phase corresponding to one k-vector used in GPA, as extracted from the Fourier transform of the corresponding image (inset, extracted k-vectors are indicated by black circles).* ***b,*** *Phase difference or GPA phase, obtained by multiplying with the original image and low-pass filtering. Overlayed is the corresponding extracted image wave in gray scale.* ***c,*** *The displacement field extracted from the GPA phase represented in panel b and those of 2 more k-vectors.* ***d,*** *Extracted local twist angle θ^*.* ***e,*** *Extracted local heterostrain. Length and color of bars indicates the magnitude ϵ of the heterostrain, direction is the direction of elongation of the atomic lattice.* ***f,g,*** *Distribution of θ^* & ϵ extracted from different areas on the sample. Bar colors correspond to colors in Figure 6.1**e**, with the remaining areas shown in Figure C.1 in Appendix C.*

them in detail [157, 158]. For this, we use adaptive geometric phase analysis (GPA), extending our earlier work on STM data of moiré patterns in TBG (see Appendix A) [88, 141, 143, 172, 173]. This method, illustrated in Figure 6.3**a-c**, yields the displacement field with respect to a perfect lattice, by multiplying the original image with complex ref-

erence waves followed by low-pass filtering to obtain the GPA phase differences, which are then converted to the displacement field. This field fully describes the distortion of the moiré lattice and allows us to extract key parameters such as the local twist angle $\theta^*(\mathbf{r})$ (see Figure 6.3**d**), and heterostrain magnitude $\epsilon(\mathbf{r})$ and direction (see Figure 6.3**e**), as described in Appendix A.6 [141, 174]. The distortions of the moiré pattern correspond directly to distortions of the atomic lattices, magnified by a factor $1/\theta$ and rotated by $90° + \theta/2$ [141, 175].

The extracted variation in twist angle and heterostrain for various regions of the sample, including those in Figure 6.1**f-i**, is summarized in Figure 6.3**f,g**, respectively. The twist angle variation within each domain is much smaller than the variation in twist angle between the separate, fold-bounded areas. Within domains, standard deviations range from 0.005° to 0.015°, i.e. significantly smaller (by a factor 3–10) than previously reported [141, 164, 165]. The strain observed is around a few tenths of a percent, which is considerable. In some domains, we find an average strain of the atomic lattice of up to $\epsilon = 0.4\,\%$. According to earlier theoretical work, such values are high enough to locally induce a quantum phase transition [160].

The variation of ϵ, as for θ^*, within the domains is significantly lower than in earlier studies. We do note that the use of GPA introduces a point spread function (PSF) that is broader than the PSF of the instrument, resulting in a lower displacement field frequency response at small scales and therefore a somewhat reduced variation. Nevertheless, the combined PSF of instrument and analysis is still comparable to other techniques that do not image the unit cell directly, allowing for a direct comparison.

We hypothesize that the difference in variations with literature stems from the relatively high temperature to which we heated the sample and measured at, combined with the relatively long averaging time of this measurement ($\geq 16\,$s for all data in Figure 6.3). The high temperature induces thermal fluctuations of the lattice (as demonstrated below), allowing the system to approach a lower energy, more homogeneous, state.

6.2.2 EDGE DISLOCATIONS

So far, we have discussed structural properties varying on the moiré length scale. However, the moiré magnification of deformations is general and extends to atomic edge dislocations (visualized in Figure 6.4**a**). This type of topological defect stems from a missing row of atomic unit cells and is characterized by an in-plane Burgers vector (in red) [176, 177]. The addition of a second (twisted) atomic layer magnifies (and rotates) the defect to an edge dislocation in the moiré lattice (illustrated in Figure 6.4**d,e**) [175]. In all cases, the location of the defect can be pinpointed by a singularity in the GPA phases and characterized by a Burgers vector (Figure 6.4**b,e**) [178].

The movement of edge dislocations in single-layer graphene and their interaction with both the in-plane and out-of-plane deformations of the atomic lattice have been studied extensively using TEM [178–180].

In our sample, we find a few such defects in the moiré lattice (See Appendix C.3). In Figure 6.4**f,g** we show an edge dislocation in a topographically flat region with $\theta = 0.63°$ (AFM data in Appendix C.4). The absence of any visible out-of-plane buckling in AFM suggests the dislocation, which in the freestanding case would be buckled [179], is flattened out by vdW adhesion between the layers and to the hBN substrate. Contrary to

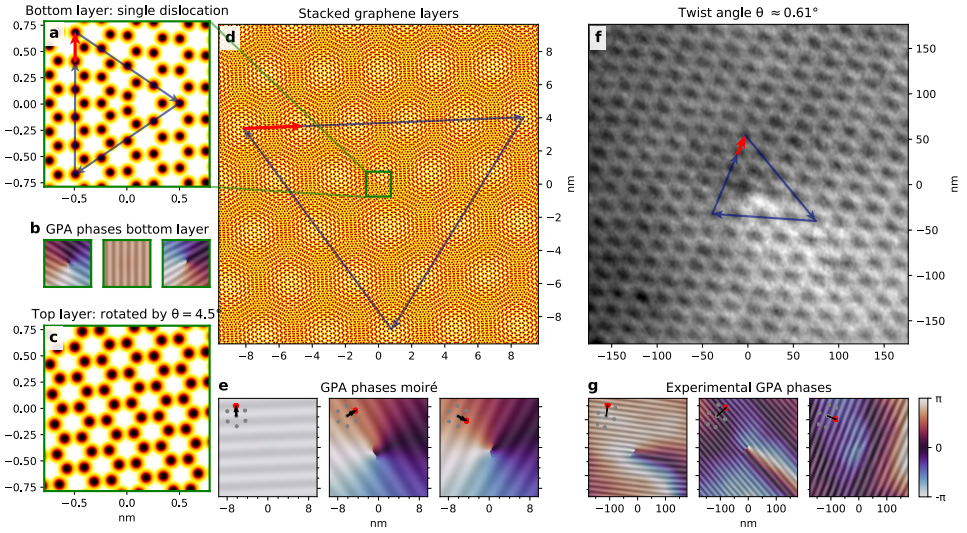

Figure 6.4: Edge dislocations in moiré systems. ***a,*** *Schematic of an edge dislocation in a single layer graphene (centered in the field-of-view), with the corresponding Burgers vector analysis (Blue arrows, Burgers vector indicated in red).* ***b,*** *GPA phases of* ***a****.* ***c,*** *Top layer without dislocation, rotated 4.5° with respect to the layer in* ***a****.* ***d,*** *Schematic of an edge dislocation of a single layer graphene in a twisted bilayer system. The green square in the center corresponds to the combination of* ***a*** *and* ***c****. The Burgers vector analysis of the moiré lattice defect is indicated by blue arrows, the resulting Burgers vector in red. Note: Both the schematics in a and d are mathematical representations of the dislocation, i.e. without taking atomic relaxation into account.* ***e,*** *GPA phases of* ***d****, exhibiting a singularity in the center. The used moiré reference vectors are indicated.* ***f,*** *LEEM image of an edge dislocation in a TBG moiré lattice with a twist angle $\theta \approx 0.63°$. The corresponding moiré Burgers vector is indicated in red.* ***g,*** *GPA phases corresponding to* ***f****.*

TEM, the low-energy electrons used for imaging here do not sputter carbon atoms, preventing creation of edge dislocations pairs and impairing movement. We do not observe creation or annihilation of edge dislocation pairs in the microscope, even at elevated measurement temperatures (500 °C) and under prolonged (i.e. hours) low-energy electron irradiation [180]. The mobility of the defects observed is low, with only one edge dislocation moving over several moiré cells between measurements, after which it remained at the same position even after a month at room temperature and reheating (See Figure C.7 in Appendix C.3). This stability suggests that the moiré lattice itself could play a role in stabilizing these defects, via a minimum of the local stacking fault energy within the moiré unit cell.

These topological dislocations break translational symmetry of the moiré lattice, which may lead to singular electronic properties on the local scale [181–183]. Specifically, a phase difference will appear between electron paths encircling the defect clockwise and counterclockwise.

6.2.3 HIGH TEMPERATURE DYNAMICS OF THE MOIRÉ LATTICE

All measurements presented so far were performed at 500 °C, to minimize hydrocarbon contamination under the electron beam.

In literature, there is concern about the graphene layers untwisting at such temperatures, due to energy differences between different rotations [112, 168]. However, no direct observation of untwisting has been presented in literature, apart from the relaxation observed above 800 °C in Ref. [106], and theoretical work indicates untwisting of large flakes would be unlikely [184]. Indeed, we see no sign of untwisting. The twist angles within the domains are stable from 100 °C up to 600 °C for all samples studied, including samples with significantly larger domains between folds, such as the one studied in Ref. [5]. However, in the current experiment a full distinction between local pinning of the moiré lattice by defects and intrinsic rotational stability of large area twisted bilayer graphene cannot be made. For that, the experiment is to be repeated on a homogeneous area, carefully isolated from the rest of the TBG sample by lithographic means.

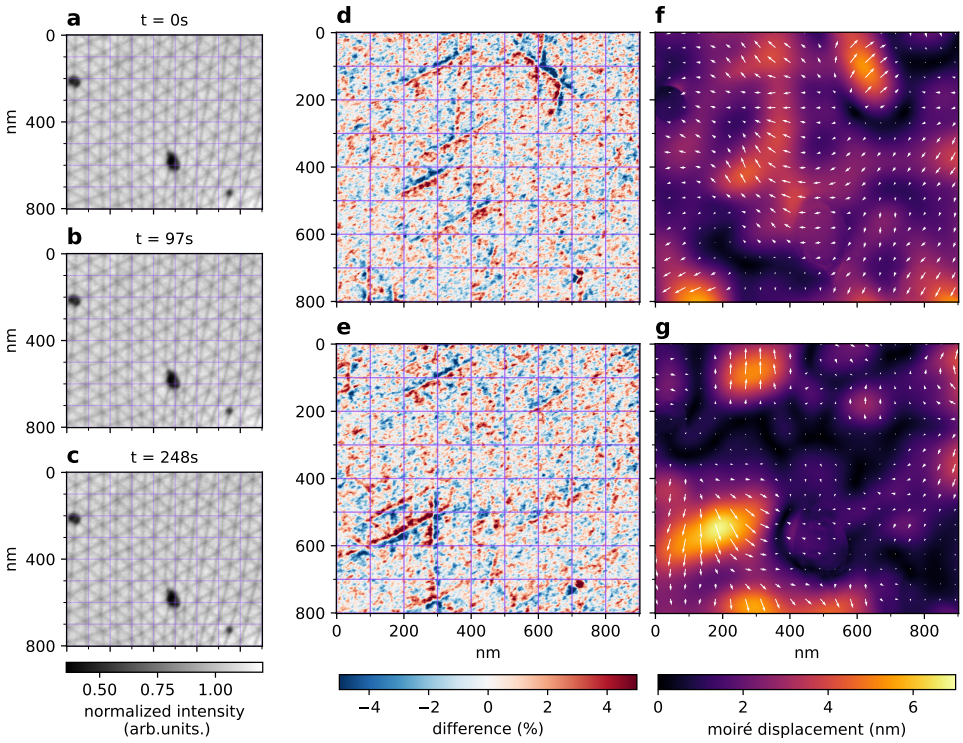

Figure 6.5: Dynamics of moiré patterns. ***a-c,*** *Three images of the same area (in the same domain as Figure 6.1* ***f****), taken minutes apart at a constant temperature of* 500 °C. *Here,* $\theta^* \approx 0.18$ *and* $\epsilon \approx 0.04\%$ *(local values as extracted by GPA can be found in Figure C.3).* ***d,e,*** *Difference of respectively* ***b*** *and* ***c*** *with* ***a****, i.e.* $t = 0$ s*, highlighting the shift of the domain boundaries.* ***f,g,*** *GPA extracted displacement of respectively* ***b,*** *and* ***c,*** *with respect to* $t = 0$ s*, with the arrows indicating the direction and amplitude magnified 8 times for visibility.*

A more subtle dynamic effect we did observe is a thermal influence on the moiré pattern. At a temperature of 500 °C, the position of the stacking domain boundaries fluctuates slightly as a function of time (see Figure 6.5**a-c**). Taking the difference of later images (Figure 6.5**b-c**) with the first image (Figure 6.5**a**), we clearly see the domain boundaries shifting (Figure 6.5**d,e**). Moreover, we can quantify these fluctuations via the difference in displacement field with respect to the image at $t = 0$ s using GPA (Figure 6.5**f,g**). Interestingly, these involve the collective movement of millions of atoms, but only over very small distances. The full dynamics are shown in Supplementary Video 1.[1]

We stress that a translation of the domain boundary by 4 nm, as observed, corresponds to a shift of less than half the width of the domain boundary itself [120, 185]. As the relative shift of the layers over the full domain boundary is a single carbon bond length, the corresponding atomic translations are less than half of that, i.e. less than 70 pm. Hence, the 'moiré magnification' makes it possible to detect these sub-Angstrom changes in TBG in real time using LEEM. Our data suggest that domain boundary displacement follows a random pattern of forward and backward steps. This indicates a possible source for the twist angle disorder observed in low(er) temperature experiments [141, 162, 164, 165]: frozen-in thermal fluctuations of the moiré lattice. The thermal fluctuations found, corresponding to ±0.005° for twist angle and ±0.02% for strain, are smaller than the extracted static deformations, though not negligible. Note that these values are damped by the intrinsic broadening of GPA and the time integration. Future experiments will focus on deducing the detailed statistics of the domain boundary dynamics versus temperature. Following these local collective excitations in time, will yield quantitative information on the energy landscape of these atomic lattice deformations within the moiré lattice. This will be important to answer the question if moiré lattices can be relaxed and homogenized using controlled annealing. If so, this would yield higher-quality magic-angle TBG devices in which charge transport is not limited by percolative effects and higher critical temperatures are reached.

6.3 CONCLUSION

This quantitative LEEM study on TBG reveals a wide variety in twist angles and strain levels in a single sample. We show that spontaneous changes in global twist angle do not occur, even at elevated temperatures, but that local collective fluctuations do take place. This suggests that high-temperature annealing causes relaxation of the local moiré lattice, reducing lattice disorder. Vice versa, this points to frozen-in thermal fluctuations as a possible source of the (significant) short-range twist angle disorder observed previously. Furthermore, this potentially offers insight into energetic aspects of the atomic lattice deformation within the moiré lattice.

We also report the observation of stable topological defects, i.e. edge dislocations, in the moiré lattice of two van der Waals layers. Combining our methods with other techniques that can access the electronic structure, such as STS, nanoARPES, and even in-situ potentiometry [6], will allow for a systematic study of the electronic properties around these defects. Finally, the methods we describe here extend beyond TBG, to any type of twisted system. Therefore, our work introduces a way of studying deformations of

[1] The supplementary video is available at https://doi.org/10.1038/s41467-021-27646-1.

moiré patterns and of connecting these to the (local) electronic properties of this exciting class of materials.

6.4 METHODS

6.4.1 SAMPLE FABRICATION

The twisted bilayer graphene sample was fabricated using the standard tear-and-stack method [4, 186]. The monolayer graphene was first exfoliated with scotch tape on to a SiO_2/Si substrate. A polycarbonate (PC)/polydimethylsiloxane (PDMS) stamp was used for the transfer process, where the PC covered only half of the PDMS surface. After the first half of the graphene flake was successfully torn and picked up, it was rotated by 1.0°. The flake was then overlapped with the bottom half and used to pick it up. The stack was then stamped on a moderately thick (~140nm) hBN flake, priorly exfoliated with PDMS on to a silicon substrate, along with the PC layer. Part of the graphene flake is deliberately put in contact with the Silicon surface for electrical contact purposes, i.e. to absorb the beam current. The whole substrate is then left in chloroform for 3 hours to dissolve the PC. All flakes were exfoliated from crystals, commercially bought from `hq graphene`[2] and the fabrication process was performed using the Manual 2D Heterostructure Transfer System sold by the same company.

6.4.2 LEEM

All LEEM measurements where performed in the ESCHER LEEM, based on the SPECS P90 [25, 27, 187]. Samples were loaded into the ultrahigh-vacuum (base pressure better than 1.0×10^{-9}mbar) LEEM main chamber and heated to 500°C at a rate not exceeding 0.45K per second (as measured by pyrometer and confirmed by IR-camera) and left at this temperature to get rid of any (polymer) residue (temperature log is shown in Figure C.10 in Appendix C). All measurements were conducted at elevated temperatures, 450°C – 500°C, unless specified otherwise. The sample was located on the substrate using photo-emission electron microscopy (PEEM) with an unfiltered mercury short-arc lamp, by comparing to optical microscopy images taken beforehand. Spectra were taken in high-dynamic-range mode and drift corrected and all images were corrected for detector artefacts, as described in Chapter 3. When needed to obtain a sufficient signal-to-noise ratio, multiple 250 ms exposures were accumulated for each image, e.g. 8 exposures (2 seconds) per landing energy in the spectra in Figure 6.1b and 16 exposures (4 seconds) at each location for the overview at 37 eV in Figure 6.1c,e.

TIME SERIES

To measure the dynamics as presented in Figure 6.5, a time series of accumulated $4 \times 250\,\text{ms} = 1\,\text{s}$ exposure images was taken back-to-back. After regular detector correction and drift correction, each image was divided by a Gaussian smoothed version of itself ($\sigma = 50$ pixels) to get rid of spatial and temporal fluctuations in electron illumination intensity. To further reduce noise, a Gaussian filter with a width of $\sigma = 1$ image ~ 1 s, was applied in the time direction before applying GPA.

[2] hq graphene, G. Meirstraat 1, 9728 TB Groningen, The Netherlands, www.hqgraphene.com

6.4.3 STITCHING

To enable high resolution, large field-of-view LEEM imaging, the LEEM sample stage [28] was scanned in a rectangular pattern over the sample, taking an image at each position, leaving sufficient overlap (2 μm steps at a 4.7 μm field-of-view). To obtain meaningful deformation information from this, care needs to be taken to use a stitching algorithm that does not introduce additional deformation, i.e. as faithfully reproducing reality as the constituting images.

To achieve this, a custom stitching algorithm tailored towards such LEEM data, was developed, as described in Appendix B and in the implementation [42].

In addition, for the composite bright field in Figure 6.1**c**, minor rotation and magnifications differences due to objective lens focus differences were compensated for. This was done by registering the stitches for different energies using a log-polar transformation based method to obtain relative rotations and magnification. Subsequently, areas where a color channel was missing, were imputed using a k-nearest neighbor lookup in a regularly sliced subset of the area with all color channels present.

6.4.4 IMAGE ANALYSIS

To quantify the large deviations in lattice shape due to the moiré magnification of small lattice distortions, we extended the GPA algorithm to use an adaptive grid of reference wave vectors, based on related to earlier work in laser fringe analysis [173].

The spatial lock-in signal is calculated for a grid of wave vectors around a base reference vector, converting the GPA phase to reference the base reference vector every time. For each pixel, the spatial lock-in signal with the highest amplitude is selected as the final signal. To avoid the problem of globally consistent phase unwrapping, the gradient of each GPA phase was directly converted to the displacement gradient tensor. More details of the used algorithm are given in Appendix A.5.

All image analysis code was written in Python, using `Numpy` [188], `Scipy` [189], `Dask` [67] and `scikit-image` [69]. The core algorithms are available as an open source Python package [88]. Throughout the development of the algorithms and writing of the paper, `matplotlib` [190, 191] was extensively used for plotting and figure creation.

6.4.5 REFLECTIVITY CALCULATIONS

The theoretical reflectivity spectra are obtained with the ab-initio Bloch-wave-based scattering method described in Ref. [117]. Details of the application of this method to stand-alone two-dimensional films of finite thickness can be found in Ref. [136]. The underlying all-electron Kohn-Sham potential was obtained with a full-potential linear augmented plane-wave method within the local density approximation, as explained in Ref. [116]. Inelastic scattering is taken into account by an absorbing imaginary potential $-iV_i$, which is taken to be spatially constant ($V_i = 0.5$ eV) over a finite slab (where the electron density is non-negligible) and to be zero in the two semi-infinite vacuum half spaces. In addition, a Gaussian broadening of 1 eV is applied to account for experimental losses.

6.4.6 DATA & CODE AVAILABILITY

The data supporting the findings of this chapter is available at 4TU.researchdata [140]. The analysis code is split in three parts: core algorithms are available at ref. [88], lattice rendering code used is available at ref. [192] and specific code to generate the figures in this paper is available at ref. [193].

REFERENCES

4. Y. Cao, V. Fatemi, S. Fang, et al. Unconventional superconductivity in magic-angle graphene superlattices. *Nature* **556,** 43–50. doi:10.1038/nature26160 (2018).
5. S. Lisi*, X. Lu*, T. Benschop*, T. A. de Jong*, et al. Observation of flat bands in twisted bilayer graphene. *Nature Physics* **17,** 189–193. doi:10.1038/s41567-020-01041-x (2021).
6. J. Kautz, J. Jobst, C. Sorger, et al. Low-Energy Electron Potentiometry: Contactless Imaging of Charge Transport on the Nanoscale. *Scientific Reports* **5,** 13604. doi:10.1038/srep13604 (2015).
25. R. Tromp, J. Hannon, A. Ellis, et al. A new aberration-corrected, energy-filtered LEEM/PEEM instrument. I. Principles and design. *Ultramicroscopy* **110,** 852–861. doi:10.1016/j.ultramic.2010.03.005 (2010).
27. R. M. Tromp, J. B. Hannon, W. Wan, A. Berghaus & O. Schaff. A new aberration-corrected, energy-filtered LEEM/PEEM instrument II. Operation and results. *Ultramicroscopy* **127,** 25–39. doi:10.1016/j.ultramic.2012.07.016 (2013).
28. A. W. Ellis & R. M. Tromp. A versatile ultra high vacuum sample stage with six degrees of freedom. *Review of Scientific Instruments* **84,** 075112. doi:10.1063/1.4813739 (2013).
29. J. I. Flege & E. E. Krasovskii. Intensity-voltage low-energy electron microscopy for functional materials characterization. *Physica Status Solidi - Rapid Research Letters* **8,** 463–477. doi:10.1002/pssr.201409102 (2014).
31. T. A. de Jong, J. Jobst, H. Yoo, et al. Measuring the Local Twist Angle and Layer Arrangement in Van der Waals Heterostructures. *physica status solidi (b)* **255,** 1800191. doi:10.1002/pssb.201800191 (2018).
34. J. Jobst, A. J. H. van der Torren, E. E. Krasovskii, et al. Quantifying electronic band interactions in van der Waals materials using angle-resolved reflected-electron spectroscopy. *Nature Communications* **7,** 13621. doi:10.1038/ncomms13621 (2016).
37. T. A. de Jong, E. E. Krasovskii, C. Ott, et al. Intrinsic stacking domains in graphene on silicon carbide: A pathway for intercalation. *Physical Review Materials* **2,** 104005. doi:10.1103/PhysRevMaterials.2.104005 (2018).
42. T. A. de Jong. *Quantitative Data Analysis for spectroscopic LEEM* version v0.2.0. 2021. doi:10.5281/zenodo.3539538.
46. R. M. Feenstra, N. Srivastava, Q. Gao, et al. Low-energy electron reflectivity from graphene. *Physical Review B* **87,** 041406. doi:10.1103/PhysRevB.87.041406 (2013).

67. Dask Development Team. *Dask: Library for dynamic task scheduling* (2016). https://dask.org.

69. S. van der Walt, J. L. Schönberger, J. Nunez-Iglesias, et al. scikit-image: image processing in Python. *PeerJ* **2,** e453. doi:10.7717/peerj.453 (2014).

88. T. A. de Jong. *pyGPA* 2021. doi:10.5281/zenodo.5589555.

106. J. S. Alden, A. W. Tsen, P. Y. Huang, et al. Strain solitons and topological defects in bilayer graphene. *Proceedings of the National Academy of Sciences* **110,** 11256–11260. doi:10.1073/pnas.1309394110 (2013).

112. Y. Cao, V. Fatemi, A. Demir, et al. Correlated insulator behaviour at half-filling in magic-angle graphene superlattices. *Nature* **556,** 80–84. doi:10.1038/nature26154 (2018).

116. E. E. Krasovskii, F. Starrost & W. Schattke. Augmented Fourier components method for constructing the crystal potential in self-consistent band-structure calculations. *Physical Review B* **59,** 10504–10511. doi:10.1103/PhysRevB.59.10504 (1999).

117. E. E. Krasovskii. Augmented-plane-wave approach to scattering of Bloch electrons by an interface. *Physical Review B* **70,** 245322. doi:10.1103/PhysRevB.70.245322 (2004).

120. H. Yoo, R. Engelke, S. Carr, et al. Atomic and electronic reconstruction at the van der Waals interface in twisted bilayer graphene. *Nature Materials* **18,** 448–453. doi:10.1038/s41563-019-0346-z (2019).

135. T. A. de Jong, T. Benschop, X. Chen, et al. Imaging moiré deformation and dynamics in twisted bilayer graphene. *Nature Communications* **13,** 70. doi:10.1038/s41467-021-27646-1 (2022).

136. E. Krasovskii. Ab Initio Theory of Photoemission from Graphene. *Nanomaterials* **11,** 1212. doi:10.3390/nano11051212 (2021).

140. T. de Jong, T. Benschop, X. Chen, et al. *Data underlying the paper: Imaging moiré deformation and dynamics in twisted bilayer graphene.* (4TU.ResearchData, 2021). doi:10.4121/16843510.

141. T. Benschop*, T. A. de Jong*, P. Stepanov*, et al. Measuring local moiré lattice heterogeneity of twisted bilayer graphene. *Physical Review Research* **3,** 013153. doi:10.1103/PhysRevResearch.3.013153 (2021).

143. M. J. Lawler, K. Fujita, J. Lee, et al. Intra-unit-cell electronic nematicity of the high-Tc copper-oxide pseudogap states. *Nature* **466,** 347–351. doi:10.1038/nature09169 (2010).

151. D. Halbertal, N. R. Finney, S. S. Sunku, et al. Moiré metrology of energy landscapes in van der Waals heterostructures. *Nature Communications* **12,** 242. doi:10.1038/s41467-020-20428-1 (2021).

155. R. Bistritzer & A. H. MacDonald. Moire bands in twisted double-layer graphene. *Proceedings of the National Academy of Sciences* **108,** 12233–12237. doi:10.1073/pnas.1108174108 (2011).

156. X. Lu, P. Stepanov, W. Yang, et al. Superconductors, orbital magnets and correlated states in magic-angle bilayer graphene. *Nature* **574,** 653–657. doi:10.1038/s41586-019-1695-0 (2019).

157. J.-B. Qiao, L.-J. Yin & L. He. Twisted graphene bilayer around the first magic angle engineered by heterostrain. *Physical Review B* **98,** 235402. doi:10.1103/PhysRevB.98.235402 (2018).

158. Z. Khatibi, A. Namiranian & F. Parhizgar. Strain impacts on commensurate bilayer graphene superlattices: Distorted trigonal warping, emergence of bandgap and direct-indirect bandgap transition. *Diamond and Related Materials* **92,** 228–234. doi:10.1016/j.diamond.2018.12.007 (2019).

159. Z. Bi, N. F. Q. Yuan & L. Fu. Designing flat bands by strain. *Physical Review B* **100,** 035448. doi:10.1103/PhysRevB.100.035448 (2019).

160. D. E. Parker, T. Soejima, J. Hauschild, M. P. Zaletel & N. Bultinck. Strain-Induced Quantum Phase Transitions in Magic-Angle Graphene. *Physical Review Letters* **127.** doi:10.1103/physrevlett.127.027601 (2021).

161. N. Tilak, X. Lai, S. Wu, et al. Flat band carrier confinement in magic-angle twisted bilayer graphene. *Nature Communications* **12.** doi:10.1038/s41467-021-24480-3 (2021).

162. E. Y. Andrei & A. H. MacDonald. Graphene bilayers with a twist. *Nature Materials* **19,** 1265–1275. doi:10.1038/s41563-020-00840-0 (2020).

163. Y. Xie, B. Lian, B. Jäck, et al. Spectroscopic signatures of many-body correlations in magic-angle twisted bilayer graphene. *Nature* **572,** 101–105. doi:10.1038/s41586-019-1422-x (2019).

164. A. Uri, S. Grover, Y. Cao, et al. Mapping the twist-angle disorder and Landau levels in magic-angle graphene. *Nature* **581,** 47–52. doi:10.1038/s41586-020-2255-3 (2020).

165. N. P. Kazmierczak, M. Van Winkle, C. Ophus, et al. Strain fields in twisted bilayer graphene. *Nature Materials,* 1–8. doi:10.1038/s41563-021-00973-w (2021).

166. T. I. Andersen, G. Scuri, A. Sushko, et al. Excitons in a reconstructed moiré potential in twisted WSe2/WSe2 homobilayers. *Nature Materials* **20,** 480–487. doi:10.1038/s41563-020-00873-5 (2021).

167. M. Koshino & Y.-W. Son. Moiré phonons in twisted bilayer graphene. *Physical Review B* **100.** doi:10.1103/physrevb.100.075416 (2019).

168. Y. Choi, J. Kemmer, Y. Peng, et al. Electronic correlations in twisted bilayer graphene near the magic angle. *Nature Physics* **15,** 1174–1180. doi:10.1038/s41567-019-0606-5 (2019).

169. H. Hibino, S. Tanabe, S. Mizuno & H. Kageshima. Growth and electronic transport properties of epitaxial graphene on SiC. *Journal of Physics D: Applied Physics* **45,** 154008. doi:10.1088/0022-3727/45/15/154008 (2012).

170. T. E. Beechem, T. Ohta, B. Diaconescu & J. T. Robinson. Rotational Disorder in Twisted Bilayer Graphene. *ACS Nano* **8,** 1655–1663. doi:10.1021/nn405999z (2014).

171. J. Mao, S. P. Milovanović, M. Anđelković, et al. Evidence of flat bands and correlated states in buckled graphene superlattices. *Nature* **584,** 215–220. doi:10.1038/s41586-020-2567-3 (2020).

172. M. J. Hÿtch, E. Snoeck & R. Kilaas. Quantitative measurement of displacement and strain fields from HREM micrographs. *Ultramicroscopy* **74,** 131–146. doi:10.1016/s0304-3991(98)00035-7 (1998).

173. Q. Kemao. Two-dimensional windowed Fourier transform for fringe pattern analysis: Principles, applications and implementations. *Optics and Lasers in Engineering* **45,** 304–317. doi:10.1016/j.optlaseng.2005.10.012 (2007).

174. A. Kerelsky, L. J. McGilly, D. M. Kennes, et al. Maximized electron interactions at the magic angle in twisted bilayer graphene. *Nature* **572,** 95–100. doi:10.1038/s41586-019-1431-9 (2019).

175. D. A. Cosma, J. R. Wallbank, V. Cheianov & V. I. Fal'ko. Moiré pattern as a magnifying glass for strain and dislocations in van der Waals heterostructures. *Faraday Discussions* **173,** 137–143. doi:10.1039/C4FD00146J (2014).

176. J. Burgers. Geometrical considerations concerning the structural irregularities to be assumed in a crystal. *Proceedings of the Physical Society (1926-1948)* **52,** 23 (1940).

177. R. Lardner. *Mathematical Theory of Dislocations and Fracture* doi:10.3138/9781487585877 (University of Toronto Press, 1971).

178. J. H. Warner, E. R. Margine, M. Mukai, et al. Dislocation-Driven Deformations in Graphene. *Science* **337,** 209–212. doi:10.1126/science.1217529 (2012).

179. O. Lehtinen, S. Kurasch, A. Krasheninnikov & U. Kaiser. Atomic scale study of the life cycle of a dislocation in graphene from birth to annihilation. *Nature Communications* **4.** doi:10.1038/ncomms3098 (2013).

180. C. Gong, A. W. Robertson, K. He, et al. Thermally Induced Dynamics of Dislocations in Graphene at Atomic Resolution. **9,** 10066–10075. doi:10.1021/acsnano.5b05355 (2015).

181. A. Mesaros, D. Sadri & J. Zaanen. Berry phase of dislocations in graphene and valley conserving decoherence. *Physical Review B* **79.** doi:10.1103/physrevb.79.155111 (2009).

182. Y.-W. Liu, Y.-N. Ren, C.-Y. Hao & L. He. Direct observation of magneto-electric Aharonov-Bohm effect in moiré-scale quantum paths of minimally twisted bilayer graphene. *Preprint at http://arxiv.org/abs/2102.00164.* http://arxiv.org/abs/2102.00164 (2021).

183. C. De Beule, F. Dominguez & P. Recher. Aharonov-Bohm Oscillations in Minimally Twisted Bilayer Graphene. *Physical Review Letters* **125,** 096402. doi:10.1103/PhysRevLett.125.096402 (2020).

184. S. Bagchi, H. T. Johnson & H. B. Chew. Rotational stability of twisted bilayer graphene. *Physical Review B* **101.** doi:10.1103/physrevb.101.054109 (2020).

185. F. Gargiulo & O. V. Yazyev. Structural and electronic transformation in low-angle twisted bilayer graphene. *2D Materials* **5,** 015019. doi:10.1088/2053-1583/aa9640 (2017).

186. K. Kim, A. DaSilva, S. Huang, et al. Tunable moiré bands and strong correlations in small-twist-angle bilayer graphene. *Proceedings of the National Academy of Sciences* **114,** 3364–3369. doi:10.1073/pnas.1620140114 (2017).

187. S. M. Schramm, J. Kautz, A. Berghaus, et al. Low-energy electron microscopy and spectroscopy with ESCHER: Status and prospects. *IBM Journal of Research and Development* **55,** 1:1–1:7. doi:10.1147/jrd.2011.2150691 (2011).

188. C. R. Harris, K. J. Millman, S. J. van der Walt, et al. Array programming with NumPy. *Nature* **585,** 357–362. doi:10.1038/s41586-020-2649-2 (2020).

189. P. Virtanen, R. Gommers, T. E. Oliphant, et al. SciPy 1.0: fundamental algorithms for scientific computing in Python. *Nature Methods* **17,** 261–272. doi:10.1038/s41592-019-0686-2 (2020).

190. J. D. Hunter. Matplotlib: A 2D Graphics Environment. *Computing in Science & Engineering* **9,** 90–95. doi:10.1109/MCSE.2007.55 (2007).

191. T. A. Caswell, M. Droettboom, A. Lee, et al. *matplotlib/matplotlib: REL: v3.3.4* 2021. doi:10.5281/zenodo.4475376.

192. T. A. de Jong. *TAdeJong/moire-lattice-generator* version 0.0.5. 2021. doi:10.5281/zenodo.5156831.

193. T. A. de Jong. *Figure generation code for "Imaging moiré deformation and dynamics in twisted bilayer graphene"* Zenodo, 2021. doi:10.5281/zenodo.5713908.